Chapter 6

Proton Induced Reaction Cross-sections

Present chapter is based on the experimental measurements of the proton induced reaction cross-sections of the ^{nat}Nb[1], ^{nat}Ag[2], and ^{nat}Ti[3] isotopes. The experiment was performed at BARC-TIFR Pelletron accelerator at Mumbai. Stack-foil activation technique followed by the off-line spectroscopic measurement of γ-rays were used for the estimation of the production cross-sections of different radionuclide. TALYS-1.9 and ALICE-2014 codes were used for the theoretical reproductions of the data. The pre-equilibrium (PE) calculations were performed within the framework of TALYS-1.9 code. The details about both the TALYS-1.9 and ALICE-2014 codes are provided in sections 4.1 and 4.3, respectively.

Publications Related to the Present Chapter...

[1] S. Parashari, S. Mukherjee, et al., Nucl. Phys. A **978** (2018) 160–172. I.F. 1.463
[2] S. Parashari, S. Mukherjee, et al., Nucl. Phys. A **979** (2018) 102–112. I.F. 1.463
[3] S. Parashari, S. Mukherjee, et al., Nucl. Phys. A **987** (2019) 128-143. I.F. 1.463

6.1 Introduction

The proton-induced reactions are of prime interest for the cross-section data measurements, which are useful for the advanced fusion/fission reactor technology, advancement of the medical/experimental accelerators, dose estimation in nuclear medicine, radiation damage studies for high energy secondary particles generated through different reaction channels during the operation of fast reactors, etc. [1,2]. In order to completely utilize the ADSs [3–9] and the ITER [10] for the green energy production in near future, light-ion induced reaction cross-section data are required with minimal uncertainties [9]. Different refractory metals are used in various reactor grade alloys [11,12] to design the structural components of a fusion reactor. These structural components get irradiated with secondary γ, n, and $p's$ during the operation of a reactor. The interaction of these high energy particles may result in long-lived radioisotopes, hydrogen production or radiation damage in the surrounding materials. Based on the discussion provided in the section 1.1, we have selected three natural occurring isotopes, niobium (Nb), silver (Ag) and titanium (Ti), for the proton-induced reaction cross-sectional studies.

The isotopes of Nb, Ag and Ti have different applications in aircraft, modern space, nuclear medicine, and, advanced nuclear reactor technologies [3–10], as they have high strength-to-weight ratio, good fatigue and creep rupture properties, small modulus of elasticity, high electrical resistivity, heat capacity, low coefficient of thermal expansion and high melting point etc [1]. Among the various applications, Nb is used in superconducting coils with tin (Sn). The toroidal coils thus made by Nb_3Sn are used in the modern experimental fusion reactors to hold and confine the shape of the plasma inside the ITER core [10]. Due to its usability in ITER and essential properties as a refractory metal, it becomes a valuable material for the ADSs, ITER and future advancement of present reactors. On the other hand, the Ti alloys are important as they possess low long-term ($<$ 10 years after shutdown) residual radioactivity, which is important in order to decrease the nuclear waste production. Ti based alloys have also been proposed and were found suitable for the application in fast reactor first wall and blanket structures [13]. Furthermore, the isotopes of silver are widely used in the industrial production of important medical radioisotopes ^{103}Pd and ^{101}Rh [14,15], which are commonly used for the treatment of prostate cancer and other types of tumors. The ^{101}Rh isotope is also used as chemotherapeutic agent. Some of the medical isotopes like; ^{43}Sc, ^{44}Sc, ^{47}Sc, are produced through the proton induced reactions on Ti. The ^{44}Sc isotope is widely used for nuclear imaging using $\beta^+ - \gamma$ coincidences [16]. In addition to this, it

is also used for pre-therapeutic imaging with the ^{47}Sc isotope. The ^{47}Sc radionuclide is also found suitable for the radio-immunotherapy [17] due to its appropriate β^- emission. The radioisotope ^{46}Sc has different applications, such as it can be used in myocardial blood flow measurements [18], as a radio-tracer to analyze Lungs [19] and a cosmogenic radionuclide for an investigation of the history of evolution of chondrites [20].

Besides the important applications of different isotopes discussed above, the proton-induced reactions with the above mentioned metals are also important for the measurements of thin layer activation, thick target yields and to provide accurate data with optimum uncertainties, so that it can be used for the charged particle beam monitoring [21–24]. The study of different reaction channels which lead to the production of different radioisotopes is also important to find the contribution of the pre-equilibrium (PE) process over the compound nucleus and direct reactions [25–27]. Taking this as the motivation, the reaction cross-sections of proton induced reactions with ^{nat}Nb, ^{nat}Ag, and ^{nat}Ti isotopes were determined. Also, the PE (%) contribution was calculated and compared within the Q-value systematics [25, 26].

6.2 Experimental Details

The measurement of excitation function of proton-induced reactions were carried out at 14UD Bhabha Atomic Research Center - Tata Institute of Fundamental Research (BARC-TIFR) Pelletron facility in Mumbai, India. Stack foil activation technique [28, 29] followed by the off-line γ-ray spectroscopy was used for the irradiated samples. A detailed description about the pelletron, stack foil activation, and the off-line γ-ray spectroscopy has been given in sections 2.1.1, 2.3.2, and 2.4, respectively. The target specifications are provided in the section 2.2. A 22 MeV proton beam of $\approx$180 nA current was used for the irradiations of all the samples. The proton beam energy was degraded along the stack of five sample foils with the help of Al foils of appropriate thicknesses. A schematic diagram of the target irradiation stack is shown in Figure 6.1. The effective proton energy after each set of degraders was calculated at the center of sample foils using the SRIM [30] software. The stack of each sample-degrader set was then irradiated in a 6 meter port of the main beam-line of the pelletron. A view of the 6 meter port is shown in Figure 2.3. A thick tantalum (Ta) collimator was used to get a proper circular shaped beam of diameter 6 mm. The beam current was constantly monitored using a Faraday cup connected to a charge integrator.

The irradiated samples were allowed to cool for a few hours to reduce the radioactive dose before recording the γ-ray spectrum. Each sample was then counted by using a pre-calibrated 80 *cc* co-axial single crystal

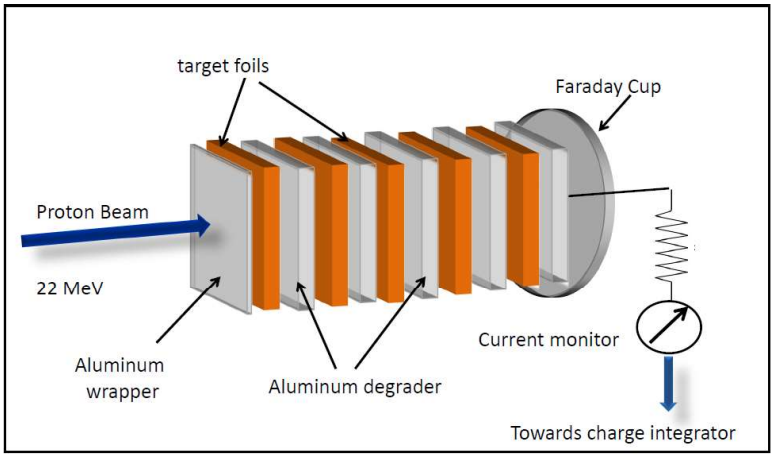

Figure 6.1: A schematic diagram of the stack foil arrangement of the target assembly

HPGe detector [4] coupled to a PC based multi channel analyzer. Different γ-ray acquisition softwares like; Maestro [31] Genie [32], FitzPeaks [33] were used to measure the activity of different γ-rays of particular interests. The irradiated samples were placed at a distance of 5 cm from the detector end cap to avoid the summing effect and to reduce the dead time. The efficiency curve for the HPGe detector at 5 cm distance is shown in Figure 2.7. The HPGe detector was calibrated with a standard ^{152}Eu source [34]. The resolution of the detector system during counting was measured as 1.82 keV at 1332 keV *gamma*-line of ^{60}Co. The counting of the samples was repeated over a long period of time extended up to days, according to the decay half-life of the reaction products. Figure 6.2 shows the recorded γ-ray spectra for [a] $p +^{nat} Nb$,. [b] $p +^{nat} Ag$, and [c] $p +^{nat} Ti$ reactions at $E_{Lab} \approx 19$ MeV.

The characteristic γ-lines shown in Figure 6.2 with their respective half-lives were used to identify the residual nuclei of interest. The spectroscopic data used in the present calculations were taken from NuDat [34] database, whereas the Q-values and the threshold energies were taken from Qtool [35], and are summarized in Table 6.1 for all the reaction residues.

6.3 Data Analysis for the ^{nat}Nb, ^{nat}Ag, and $^{nat}Ti(p,x)$ reactions

The excitation function for the proton-induced reactions on ^{nat}Nb, ^{nat}Ag, and ^{nat}Ti have been measured at five incident energies within the 10-22

[4] Details about the HPGe detector are given in section 2.4.1

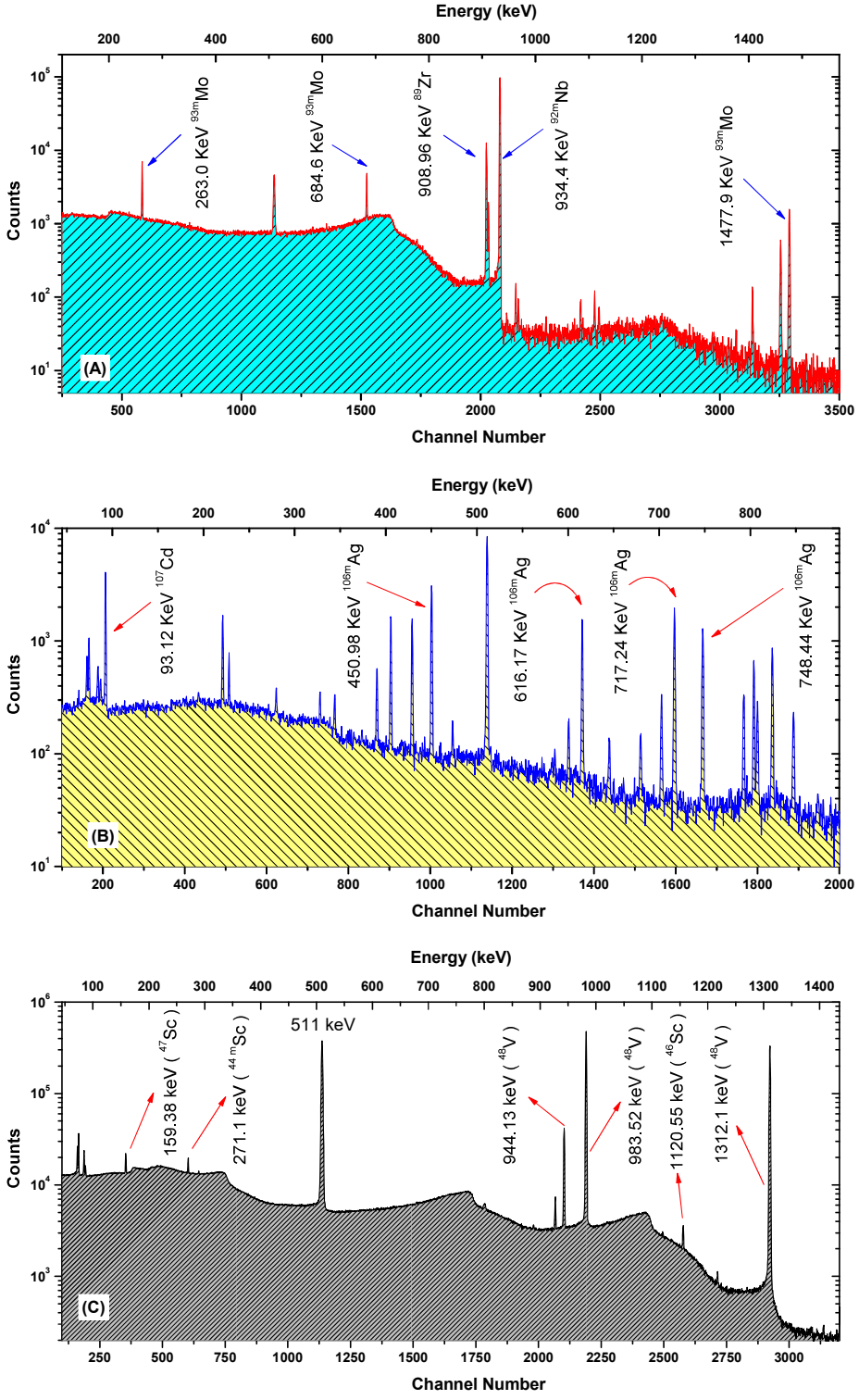

Figure 6.2: Typical $\gamma-$ray energy spectrum obtained from the interaction of (from top) [A] $p+^{nat}Nb$ at $E_{Lab} \approx 19$ MeV, [B] $p+^{nat}Ag$ at $E_{Lab} \approx 19$ MeV, and [C] $p+^{nat}Ti$ at $E_{Lab} \approx 19$ MeV

Table 6.1: List of the identified residues in the proton induced ^{nat}Nb, ^{nat}Ag and ^{nat}Ti reactions with their spectroscopic data [34,35].

Nuclide	$T_{1/2}$	Deacy Mode	E_γ (keV)	I_γ (%)	Reaction	E_{Th} (MeV)
^{93m}Mo	6.85 h	IT (99.88 %)	263.05	57.40 ± 0.11	$^{93}Nb(p,n)$	1.20
		$\epsilon(0.12\%)$	684.69	99.9 ± 0.8		
			1477.14	99.10 ± 0.11		
^{93g}Mo	4.0×10^3 y	$\epsilon(100\%)$	-	-	-	-
^{92m}Nb	10.15 d	$\epsilon(100\%)$	934.44	99.15	$^{93}Nb(p,pn)$	9.06
^{92g}Nb	3.47×10^7 y	$\epsilon(100\%)$	934.5	74.0 ± 0.11		
		$\beta^+(< 0.05\%)$				
^{89m}Zr	4.16 m	IT(93.77%)	587.83	89.62	$^{93}Nb(p,\alpha n)$	5.60
^{89g}Zr	78.41 h	$\epsilon(100\%)$	909.15	99.14		
^{107}Cd	6.50 h	$\varepsilon(100\%)$	93.12	4.8 ± 0.3	$^{107}Ag(p,n)$	2.21
					$^{109}Ag(p,3n)$	18.82
^{106g}Ag	23.96 m	$\varepsilon(99.5\%)$	-	-	-	-
		$\beta^-(< 1\%)$	-	-	-	-
^{106m}Ag	8.28 d	$\varepsilon(100\%)$	450.98	28.2 ± 0.7	$^{107}Ag(p,d)$	7.37
			616.17	21.6 ± 0.6	$^{107}Ag(p,pn)$	9.62
			717.24	28.9 ± 0.8		
			748.44	20.6 ± 0.6		
^{48}V	15.97 d	$\varepsilon(100\%)$	983.52	99.98	$^{47}Ti(p,\gamma)$	—
			1312.1	97.5	$^{48}Ti(p,n)$	4.8
					$^{49}Ti(p,2n)$	13.20
^{47}Sc	3.349 d	$\beta^-(100\%)$	159.38	68.3	$^{48}Ti(p,2p)$	11.68
					$^{49}Ti(p,^3He)$	12.11
					$^{50}Ti(p,\alpha)$	2.28
^{46}Sc	83.79 d	$\beta^-(100\%)$	889.28	99.98	$^{47}Ti(p,2p)$	10.69
			1120.55	99.99	$^{48}Ti(p,^3He)$	14.67
					$^{49}Ti(p,\alpha)$	1.98
					$^{50}Ti(p,n\alpha)$	13.13
^{44g}Sc	3.93 h	$\varepsilon(100\%)$	—	—	$^{47}Ti(p,\alpha)$	2.30
^{44m}Sc	58.61 h	$IT(98.8\%)$	271.1	86.7	$^{48}Ti(p,n\alpha)$	14.17
		$\varepsilon(1.2\%)$				

$m \rightarrow minute, h \rightarrow hour, d \rightarrow day, y \rightarrow year$

MeV range. At such high incident proton energies, several reaction channels populate and result in different residues. In the present work, we have identified three residues in the $^{nat}Nb(p,x)$ reactions, two residues in $^{nat}Ag(p,x)$ reactions and four residues in $^{nat}Ti(p,x)$ reactions in the energy region from 10 to 22 MeV. The characteristic γ-lines of each populated residue were used to calculate the reaction cross-sections using the following expression[5],

[5]A detailed derivation for the reaction cross-section has been given in section 3.1

$$\sigma_R = \frac{C_{obs}\lambda(\frac{T_R}{T_L})}{N_0\phi I_\gamma K\epsilon(1-e^{-\lambda t_i})(e^{-\lambda t_c})(1-e^{-\lambda T_L})} \tag{6.1}$$

where σ_R is the reaction cross-section, C_{obs} is the photo peak count of the γ-line of interest, T_R and T_L are the clock time and the live time for the counting of the spectrum, λ is the decay constant, I_γ is the branching ratio for the each γ-ray taken from Ref. [34], N_o is the total number of the target nuclei in the sample, ϵ is the detector efficiency, ϕ is the proton flux and $K = [1 - exp(-\mu d)]/(\mu d)$ is the correction factor for the self absorption of the γ-rays in the sample thickness 'd' with absorption coefficient μ [36].

All the residues were identified using the spectroscopic properties of their characteristic γ-lines and by following their half-lives [34] from different counting statistic data. Three residues, ^{93m}Mo, ^{92m}Nb, and ^{89g}Zr, populated through (p, n), (p, pn) and (p, αn) reaction channels, respectively, in the interaction of proton with ^{nat}Nb target for the incident energies of 11.56 ± 0.23, 14.13 ± 0.20, 16.98 ± 0.17, 19.53 ± 0.16, and 21.85 ± 0.14 MeV. The radionuclide ^{93}Mo has a ground state ($t_{1/2} \rightarrow 4.0 \times 10^3$ years) and a metastable state ($t_{1/2} \rightarrow 6.85$ hours). The γ-lines of 263.05 keV (57.4%), 684.69 keV (99.8%) and 1477.14 keV (99.1%) were used to evaluate the cross-sections for the ^{93m}Mo residue. Similarly, the ^{92m}Nb isotope has a short half-life of 10.15 hours, compared to its ground state ($T_{1/2} = 3.47$ years). This prevents the intermixing of events coming from the common γ-lines of both the ground as well as the metastable states. Therefore, a γ-ray spectrum recorded after a short cooling time was used to estimate the cross-sections by identifying 934.44 keV (99.15%) γ-line. The radionuclide ^{89}Zr also possesses both ground and metastable states with half-lives of 78.41 hours and 4.18 min respectively. Therefore, in this case, we have identified only the ground state of ^{89}Zr by using the 909.15 keV (100%) γ-line.

The mid-point energy for the Ag foils were found to be 11.13 ± 0.28, 13.90 ± 0.23, 16.77 ± 0.20, 19.48 ± 0.18, and 21.82 ± 0.17 MeV, respectively. In the present study, we have identified two reaction residues, ^{107}Cd and ^{106m}Ag. The residue ^{107}Cd may populate by $^{107}Ag(p,n)$ and/or $^{109}Ag(p,3n)$ reaction channels which have thresholds of 2.21 and 18.82 MeV, respectively. On the other hand, the residue ^{106m}Ag, may populate through the $^{107}Ag(p,d)$ and $^{107}Ag(p,pn)$ reaction channels having the threshold of 7.37 and 9.62 MeV, respectively. These residues were identified by following the half-lives of their characteristic γ-lines [34]. A γ-line of 93.12 ± 0.02 keV (4.8 ± 0.3%) was used to identify radionuclide ^{107}Cd ($t_{1/2} \rightarrow 6.50 \pm 0.02$ hours) and to evaluate the cross-sections for the $^{nat}Ag(p,x)^{107}Cd$ reactions. However, ^{106}Ag has both ground as well as the meta-stable state. The ground state of ^{106}Ag ($t_{1/2} \rightarrow 23.96 \pm 0.04$ minutes) has a short half-life

as compared to its metastable state (8.28 ± 0.02 days). Four $\gamma - lines$ of 450.98 ± 0.02 ($28.2 \pm 0.7\%$), 616.17 ± 0.03 ($21.6 \pm 0.6\%$), 717.24 ± 0.09 ($28.9 \pm 0.8\%$) and 748.44 ± 0.11 ($20.6 \pm 0.6\%$) keV, respectively, were used for the measurement of the cross-sections for the $^{nat}Ag(p,x)^{106m}Ag$ reactions. The final cross-sections for the $^{nat}Ag(p,x)^{106m}Ag$ reactions were opted by taking the weighted average of the cross-sections from each of the four γ-lines.

The energy of the incident proton beam (E_p) at the center of ^{nat}Ti foils were found to be 12.94 ± 0.07, 15.05 ± 0.07,17.56 ± 0.06, 19.84 ± 0.05, and 21.95 ± 0.05 MeV, respectively. In the present case, four reaction products; ^{48}V, ^{47}Sc, ^{46}Sc, and ^{44m}Sc, were found to be produced in the $p +^{nat} Ti$ reaction. The residue ^{48}V ($t_{1/2} = 15.97$ days) [34] can be produced through three different channels $^{47}Ti(p,\gamma)$, $^{48}Ti(p,n)$, and $^{49}Ti(p,2n)$ depending on the respective reaction threshold values. The counting statistics of two prominent γ-lines, 983.52 (99.98%) and 1312.1 keV (97.5%) [34] were used separately for the measurement of the production cross-section of the ^{48}V isotope. The final cross-section of the $^{nat}Ti(p,x)^{48}V$ reaction was measured by taking the weighted average of the results of two γ-lines. Similarly, the production cross-sections were measured for the ^{47}Sc and ^{46}Sc reaction residues. The contributing reaction channels from different isotopes of Ti into the ^{47}Sc and ^{46}Sc residues are listed in Table 6.1.

6.3.1 Uncertainties in the Measurement

The errors in the measured production cross-sections may arise mainly due to following reasons;

- Since we have used the Faraday cup for the measurement of the proton flux, therefore, the small fluctuations in the beam current may result in the variation of incident flux. Proper care has been taken to minimize the beam current fluctuations and the beam profile was monitored on small intervals to minimize the statistical fluctuations as well.

- Non-uniform thickness of samples may lead to the uncertainty in the determination of the number of target nuclei. To reduce this error, all the samples were cut off from a large foil. It is estimated that the error in the thickness of the samples as $\leq 1\%$.

- Uncertainty in the determination of geometry dependent efficiency of γ-spectrometer. The error in the efficiency determination due to the statistical fluctuations in the counting statistics has been estimated to be $\leq 1\%$ for the present measurements.

- The loss of the product nuclei recoiling out of the sample may introduce large errors in the measured cross-sections. In order to prevent it, all the samples were wrapped in thin aluminum catcher foil and were counted along with the wrapper.

- The dead time of the spectrometer may also introduce errors in the measured cross-sections. The dead time of the spectrometer in the present measurements has been kept $\leq$ 5% by suitably adjusting sample-detector distance.

The production cross-section using the equation 6.1 were measured for each residue populated in the proton induced reactions of ^{nat}Nb, ^{nat}Ag, and ^{nat}Ti. The measured cross-sections are listed in Tables 6.2, 6.3, and 6.4, respectively.

Table 6.2: The experimentally measured cross-sections for the identified residues in the $p +^{nat} Nb$ interaction.

Proton Energy (E_p)	Cross-Section (mb)		
(MeV)	^{93m}Mo	^{92m}Nb	^{89g}Zr
11.59 ± 0.46	22.31 ± 1.16	0.113 ± 0.006	-
14.13 ± 0.40	22.89 ± 1.12	5.56 ± 0.25	0.023 ± 0.002
16.98 ± 0.35	10.54 ± 0.75	41.36 ± 2.93	2.83 ± 0.18
19.53 ± 0.32	5.58 ± 0.32	75.25 ± 3.37	13.24 ± 0.59
21.85 ± 0.29	4.09 ± 0.27	91.17 ± 5.74	24.54 ± 1.59

Table 6.3: The experimentally measured cross-sections for the identified reaction residues in the $p +^{nat} Ag$ interaction.

Proton energy (E_p)	Cross-Section (mb)	
(MeV)	^{107}Cd	^{106m}Ag
11.13 ± 0.28	222.52 ± 20.44	-
13.90 ± 0.23	175.59 ± 16.85	0.218 ± 0.215
16.77 ± 0.20	47.76 ± 4.63	11.21 ± 0.93
19.48 ± 0.18	28.45 ± 2.25	$30.57 \pm 0.2.65$
21.82 ± 0.17	104.18 ± 9.89	52.14 ± 4.74

Table 6.4: The experimentally measured reaction cross-sections for the identified residues in the $p + ^{nat}Ti$ interaction.

Proton Energy (E_p)	Cross-Section (mb)			
(MeV)	^{48}V	^{47}Sc	^{46}Sc	^{44m}Sc
12.94 ± 0.07	457.92 ± 42.44	1.06 ± 0.07	1.58 ± 0.12	0.837 ± 0.069
15.05 ± 0.07	328.54 ± 28.31	1.18 ± 0.08	2.09 ± 0.16	1.03 ± 0.08
17.56 ± 0.06	158.34 ± 14.23	2.98 ± 0.18	3.43 ± 0.22	1.42 ± 0.11
19.84 ± 0.05	93.46 ± 8.9	6.96 ± 0.52	4.22 ± 0.34	1.35 ± 0.09
21.95 ± 0.05	67.76 ± 5.8	10.79 ± 0.83	5.49 ± 0.45	3.54 ± 0.23

6.3.2 Theoretical Calculation within the Framework of TALYS-1.9 and ALICE-2014 codes

In the present work, the experimental data were measured with the theoretical results from TALYS-1.9 [37] and ALICE-2014 [38, 39] codes[6]. In the code TALYS-1.9 [37], all the six level density models (ldmodel 1-6)[7] [40–45] have been tested for the comparison of the measured data. Similarly, the level density models present in ALICE-2014[8] [38, 39] were used to find a better agreement of theoretical results with the measured data. The pure compound nucleus contribution was calculated by using different pre-equilibrium models (preeqmodel 1-4)[9] [46–48] present in TALYS-1.9 as well as by switching off the pre-equilibrium calculations in the input description. The PE contribution (%) [49] can be defined as,

$$PE(\%) = \frac{(ER_{tot} - ER_{CN})}{ER_{CN}} \times 100 \tag{6.2}$$

where, ER_{tot} is the total production cross-section and ER_{CN} is the pure CN cross-section of an evaporation residue. The pure CN and PE+CN results for different residues are plotted in respective figures. A PE contribution (%) is also calculated to check the effects of PE process with the incident particle energies. In addition to the above, pre-equilibrium fraction has also been compared among the (n, p) channels of ^{nat}Nb, ^{nat}Ag, and ^{nat}Ti reactions.

[6] A detailed discussion about the codes are given in section 4.

[7] The details of each of the model code is provided in the section 4.1.

[8] All the ingredients of ALICE-2014 code has been discussed in section 4.3.

[9] See section 4.1.2

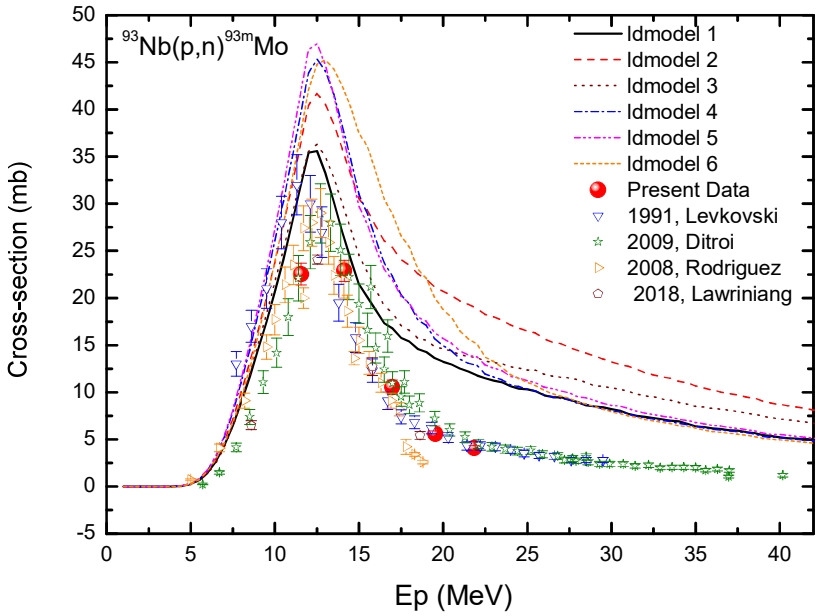

Figure 6.3: Excitation function of the $^{93}Nb(p,n)^{93m}Mo$ reaction. The comparison of the present and the literature data [50–55] with different level density model parameters in TALYS-1.9 [37].

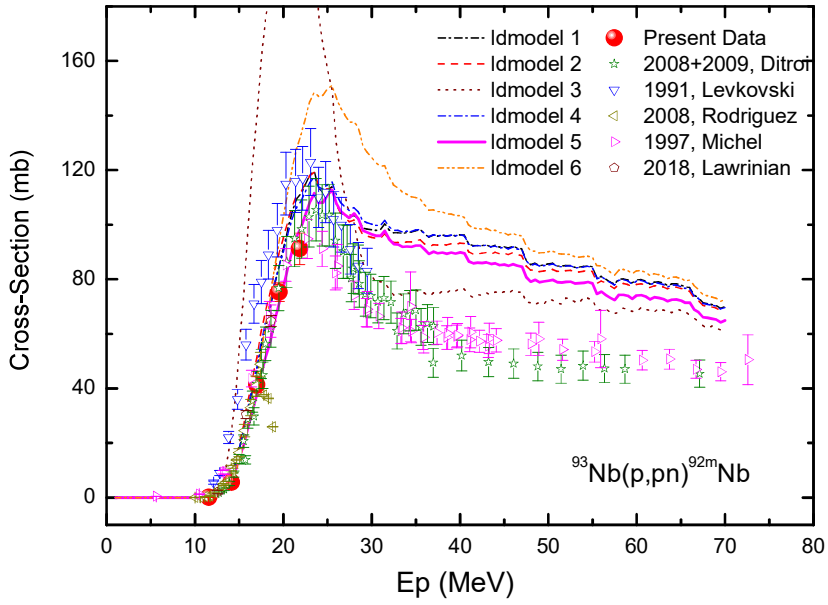

Figure 6.4: Excitation function of the $^{93}Nb(p,pn)^{92m}Nb$ reaction.The comparison of the present and the literature data [50–55] with different level density model parameters in TALYS-1.9 [37].

6.4 Excitation Functions

The excitation functions of the proton-induced reactions with ^{nat}Nb, ^{nat}Ag, and ^{nat}Ti targets were measured by using the equation 6.1. The measured cross-sections are given in Tables 6.2, 6.3, and 6.4. The measured cross-sections were compared with TALYS-1.9 [37] and ALICE-2014 [38,39] theoretical codes. The comparison between the measured data and the theoretical reproductions are plotted in Figures 6.3-6.15. The present results show fair agreement with the literature and theoretical data. A detailed discussion is provided in the following subsections, 6.4.1, 6.4.2, and, 6.4.3, for the radioisotopes populated in each interaction, separately. The effect of PE process and its contribution to the formation of the residues is also discussed in section 6.5.

6.4.1 The $^{nat}Nb(p,x)$ reaction cross-sections

The measured reaction cross-sections compared with the theoretical reproductions using different level density models (ldmodel 1-6 [40–45]) in TALYS-1.9 [37] along with the literature data [50–55] are plotted in Figures 6.3-6.5. The excitation function of the $^{nat}Nb(p,n)^{93m}Mo$ reaction is shown in Figure 6.3. It can be seen from the figure, that the measured data are in agreement with the literature data [50–55]. Minor discrepancies can also be found among the data from Ditroi et al. [50], Rodriguez et al. [51], and Levkovski [53] for the incident proton energies below 14 MeV. Since the measurements are strongly dependent on the proton flux, therefore, discrepancies of such order can arise due to the use of different monitor reactions. It can also be seen from the figure that the ldmodel 1 [40], which stands for the Fermi gas model [40][10], has been found successful to reproduce the experimental data up to 15 MeV. As the incident energy increases beyond this point, the TALYS-1.9 starts to over-predict the data. The over-prediction of data may be due to involvement of the pre-equilibrium and direct reactions at energies above 15 MeV.

The excitation function of $^{nat}Nb(p,pn)$ reaction is shown in Figure 6.4. It can be observed from the figure that the measured data are in agreement with the literature data. A constant enhancement in the reported cross-section by Levkovski [53] from the rest of the experimental data can also be noticed, which is similar to the Figure 6.3. On the other hand, the data from Ditroi et al. [50], Michel [54] and Lawriniang et al. [55] were found to be consistent except a few data points above 40 MeV. It is also noticed that the TALYS-1.9 was only found to reproduce the trend of experimental data.

[10]Fermi Gas model is used by the TALYS default input description

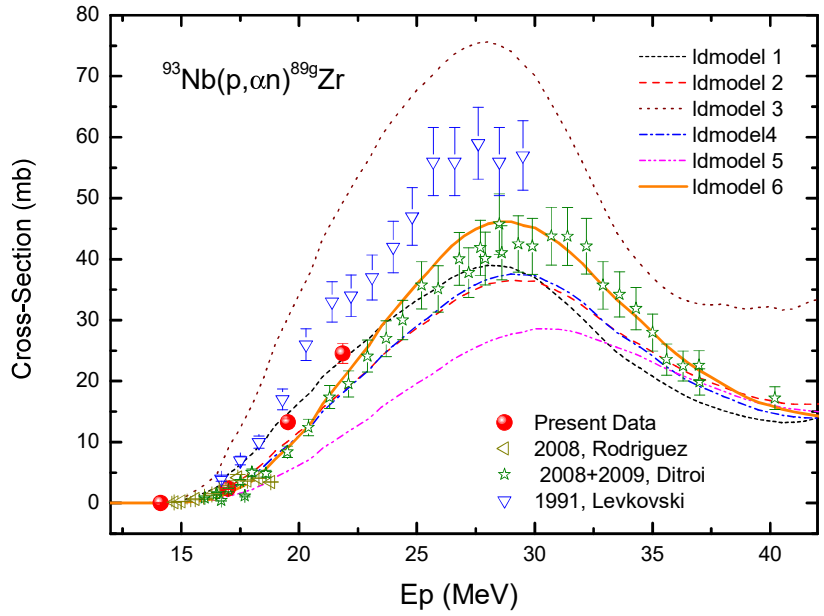

Figure 6.5: Excitation function of the $^{93}Nb(p,\alpha n)^{89g}Zr$ reaction. The comparison of the present and the literature data [50–55] with different level density model parameters in TALYS-1.9 [37].

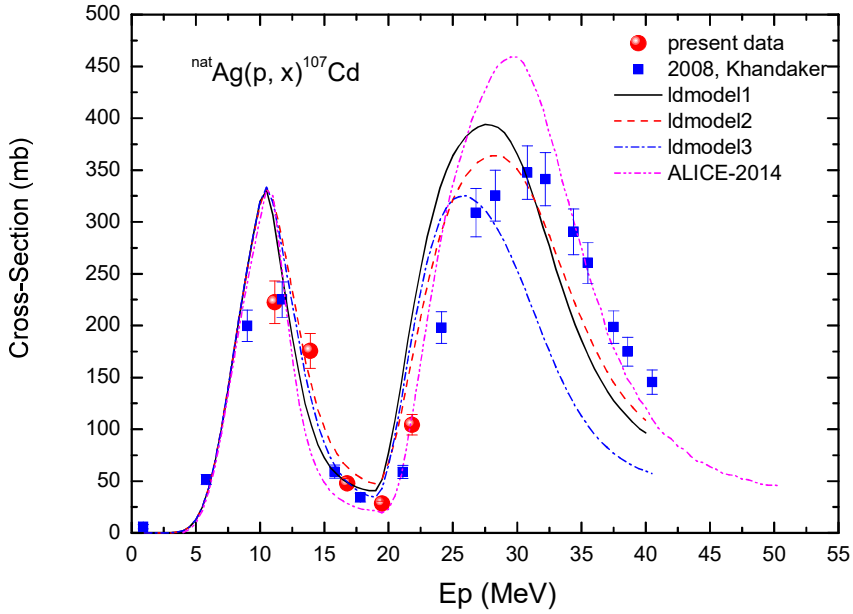

Figure 6.6: The comparison of the excitation function of the $^{nat}Ag(p,x)^{107}Cd$ reaction with the literature data [56] and the theoretical model codes TALYS-1.9 [37] and ALICE-2014 [38, 39]

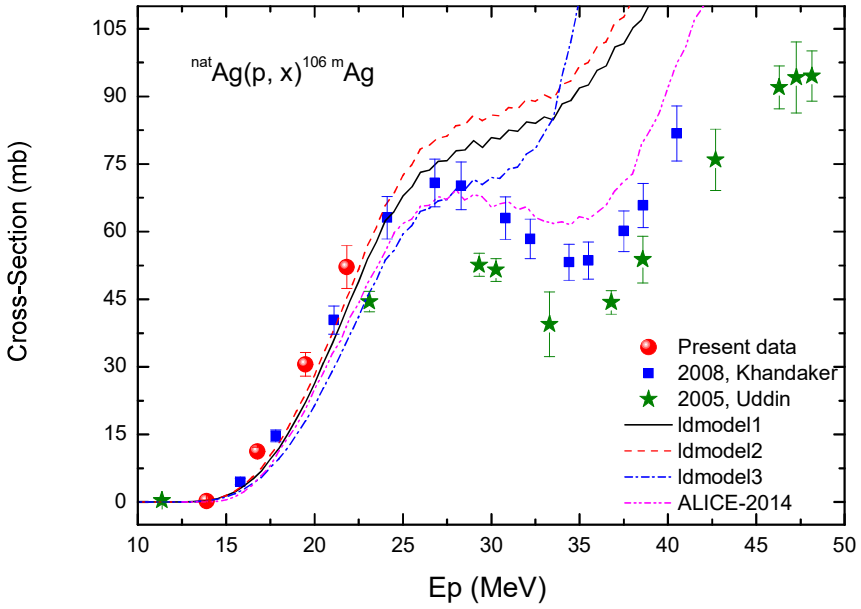

Figure 6.7: The comparison of the excitation function of the $^{nat}Ag(p,x)^{106m}Ag$ reaction with the literature data [56] and the theoretical model codes TALYS-1.9 [37] and ALICE-2014 [38,39]

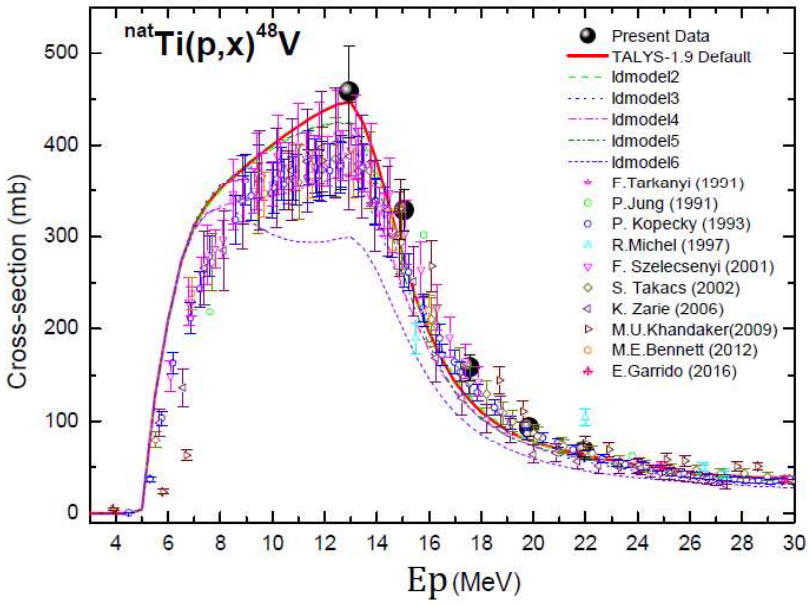

Figure 6.8: Excitation function of $^{nat}Ti(p,x)^{48}V$ reaction. The comparison of the present and the literature data [63–65,68–73,75] with different level density model parameters (ldmodel 1-6) [40–45] in TALYS-1.9 [37].

However, ldmodel-5 [44], which uses the microscopic level densities from the Hilaire's Tables, was found to reproduce best fit among the different ldmodels of the code. Similar to the previous case, TALYS-1.9 was found to over-predict the cross-sections above 25 MeV, which may again refer to the over-prediction of the PE and direct reaction cross-sections in (p, pn) channel.

The excitation function of $^{nat}Nb(p,\alpha n)^{89g}Zr$ reaction is shown in Figure 6.5. It can be seen from the figure that the present results are in agreement with the data from Ditroi et al. [50] and Rodriguez et al. [51]. However, the data from Levkovski [53] are slightly more enhanced as compared to that from Ditroi et al. [50] and the present results. The ldmodel 1 [40] and 6 [45] from TALYS-1.9, were found suitable to fit the measured data. However, other ldmodels [41–44] present in TALYS-1.9 were only found to reproduce an overall trend of the data.

6.4.2 The $^{nat}Ag(p,x)$ reaction cross-sections

The excitation function for the $^{nat}Ag(p,x)^{107}Cd$ reaction is plotted in Fig. 6.6 and are given in Table 6.3. As shown in the figure, there is only one experimental study that has been carried out by Khandaker et al., [56] using natural silver as target. The present results are in accordance with this literature data [56] and from the EXFOR [57] compilation. Two distinct peaks can be observed in the Fig. 6.6, in which, the first corresponds purely to the (p, n) channel from the ^{106}Ag isotope, however, both the $^{106}Ag(p,n)$ and $^{109}Ag(p,3n)$ channels contribute to the later. The valley around the 20 MeV proton energies corresponds to the opening of the $^{109}Ag(p,3n)$ reaction channel around 18 MeV. The nuclear model codes; TALYS-1.9 [37] and ALICE-2014 [38, 39] were found to be successful in reproducing the reaction cross-section data fairly well up to 25 MeV. Beyond 25 MeV, a slight departure of theoretical values can be observed from the measured values. The broadening of the second peak in the Fig. 6.6, may be due to the admixture of the (p, 3n) channel coming from the ^{109}Ag, which can be fitted by using a rigorous calculations in TALYS-1.9. The Back-shifted Fermi gas model (ldmodel 2) [41], among the different level density models used for the present calculations, was found to be successful in order to reproduce the experimental data. The ALICE-2014 [38, 39] code also follows a similar trend except for the second peak which corresponds to the $^{109}Ag(p,3n)^{107}Cd$ reaction channel.

The excitation function of the $^{nat}Ag(p,x)^{106m}Ag$ reaction is shown in Fig. 6.7. It can be observed from the figure 6.7 that the present results are in agreement with the literature data [56, 60]. The data from Khandaker et al.

[56] were found to be enhanced to a small degree. The minor disagreement between both the data [56, 60] may be attributed to the use of different monitor reactions. The theoretical results from TALYS-1.9 [37] were found to be significantly higher than the experimental results for energies above 25 MeV. On the other hand, the experimental results were very well reproduced by the ALICE-2014 [38,39] calculations in the incident energy range of 10-22 MeV. The different level density models from TALYS-1.9 [37] have also been tested for the present case, however, the results followed the trend of default values. Furthermore, the ALICE-2014 [38,39] model code calculations were found to be more accurate in the theoretical calculations of the reaction cross-section data for an almost entire range of the proton energies under consideration.

6.4.3 The $^{nat}Ti(p,x)$ reaction cross-sections

The excitation function of the $^{nat}Ti(p,x)^{48}V$ reaction was measured at five incident proton energies, 21.95 ± 0.05, 19.84 ± 0.05, 17.56 ± 0.06, 15.05 ± 0.07, and, 12.94 ± 0.07 MeV respectively. The measured cross-sections are shown in Table 6.4. A comparison have also been made with the literature data [63–65,68–73,75], and the theoretical model code reproductions from TALYS-1.9 [37] and ALICE-2014 [38,39]. It can be observed from figure 6.8 that the present results are in accordance with the literature data for the entire range of the incident particle energies under consideration. The TALYS-1.9 input level density models were also find successful in order to reproduce the reaction data except the ldmodel 6 [45], which was found to under-predict the data for the 6-14 MeV proton energies. On the other hand, Fig. 6.9 presents the comparison among the theoretical data using the Fermi Gas and Kataria-Ramamurthy level density models (at level density parameter K=9 [76]) of ALICE-2014 [38,39] with TALYS-1.9 [37] default (Fermi Gas model) [40], present results and the literature data. We can observe from Fig. 6.9 that ALICE-2014 [38,39] model code was found to be over-predicting the reaction cross-section data by using the similar Fermi Gas model as that of TALYS-1.9 [37]. However, the Kataria-Ramamurthy level density model was found to under-predict the cross-section data for the incident proton energies from threshold to 14 MeV. Moreover, the Obninsk level density model predicted the trend of the cross-section data successfully. The ambiguity between the ALICE-2014 [38,39] and TALYS-1.9 [37] data values using different level density models may be attributed to the level density parameter values set as default in both the codes.

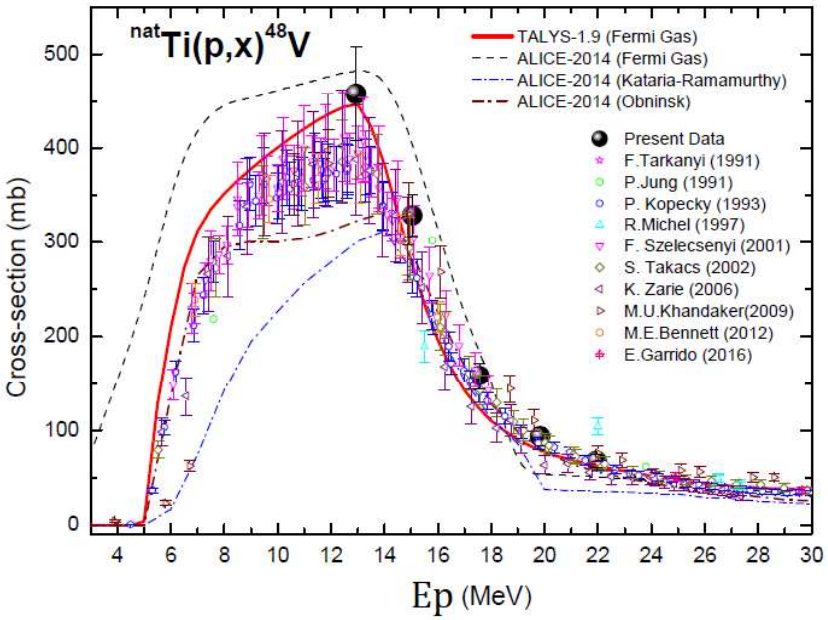

Figure 6.9: Excitation function of $^{nat}Ti(p,x)^{48}V$ reaction. The comparison of the present and the literature data [63–65, 68–73, 75] with different level density model parameters (Fermi Gas and Kataria-Ramamurthy) in ALICE-2014 [38, 39] and TALYS-1.9 [37] default values.

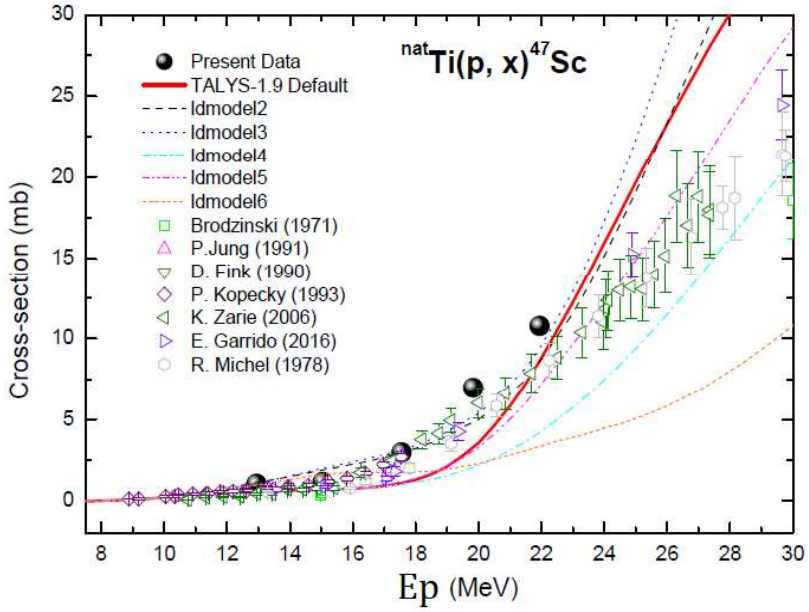

Figure 6.10: Excitation function of $^{nat}Ti(p,x)^{47}Sc$ reaction. The comparison of the present and the literature data [61–64, 66, 71, 75] with different level density model parameters (ldmodel 1-6) [40–45] in TALYS-1.9 [37].

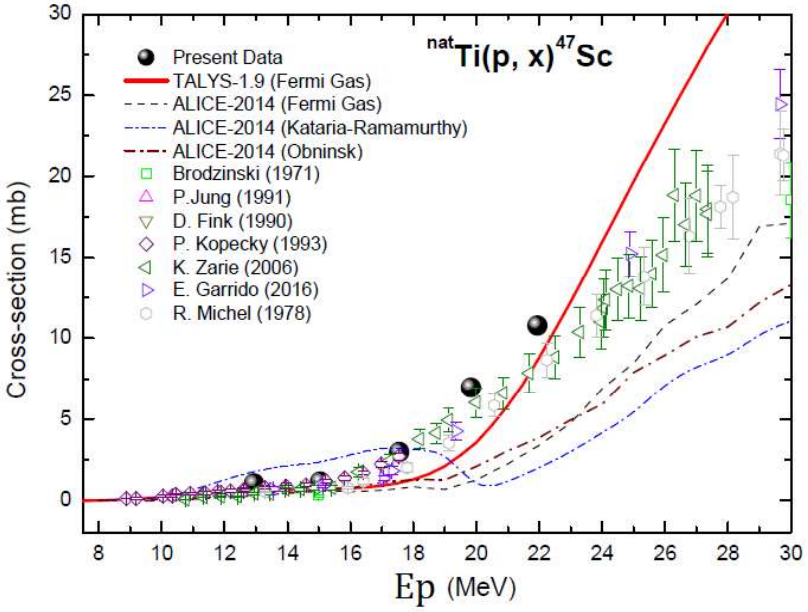

Figure 6.11: Excitation function of $^{nat}Ti(p,x)^{47}Sc$ reaction. The comparison of the present and the literature data [61–64, 66, 71, 75] with different level density model parameters (Fermi Gas and Kataria-Ramamurthy) in ALICE-2014 [38, 39] and TALYS-1.9 [37] default values.

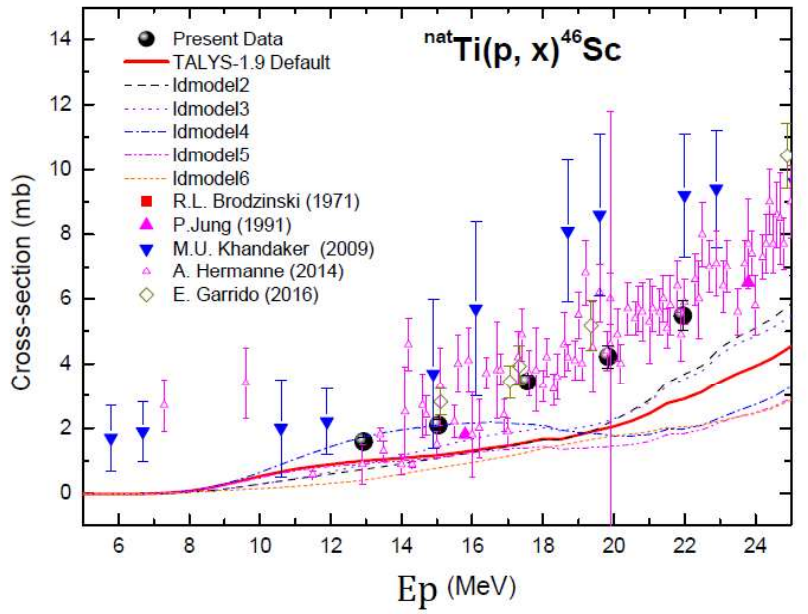

Figure 6.12: Excitation function of $^{nat}Ti(p,x)^{46}Sc$ reaction. The comparison of the present and the literature data [61, 63, 72, 74, 75] with different level density model parameters (ldmodel 1-6) [40–45] in TALYS-1.9 [37].

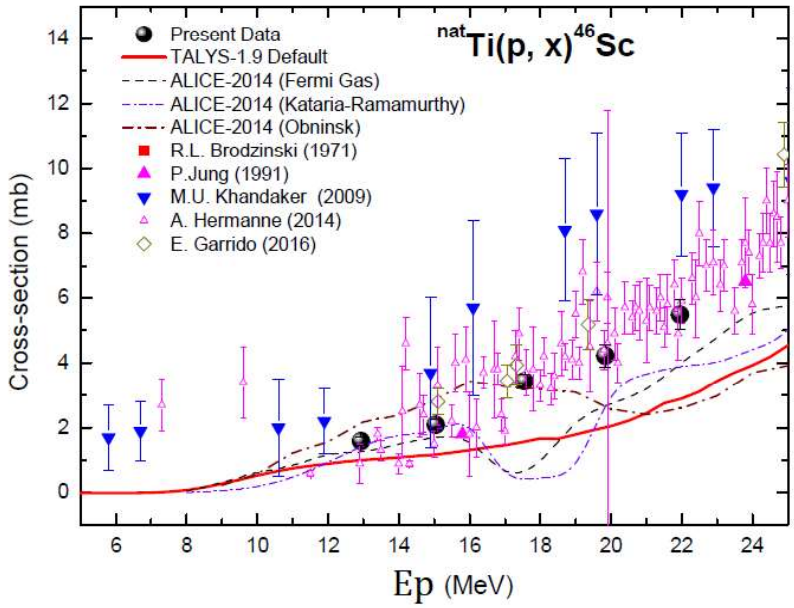

Figure 6.13: Excitation function of $^{nat}Ti(p,x)^{46}Sc$ reaction. The comparison of the present and the literature data [61, 63, 72, 74, 75] with different level density model parameters (Fermi Gas and Kataria-Ramamurthy) in ALICE-2014 [38, 39] and TALYS-1.9 [37] default values.

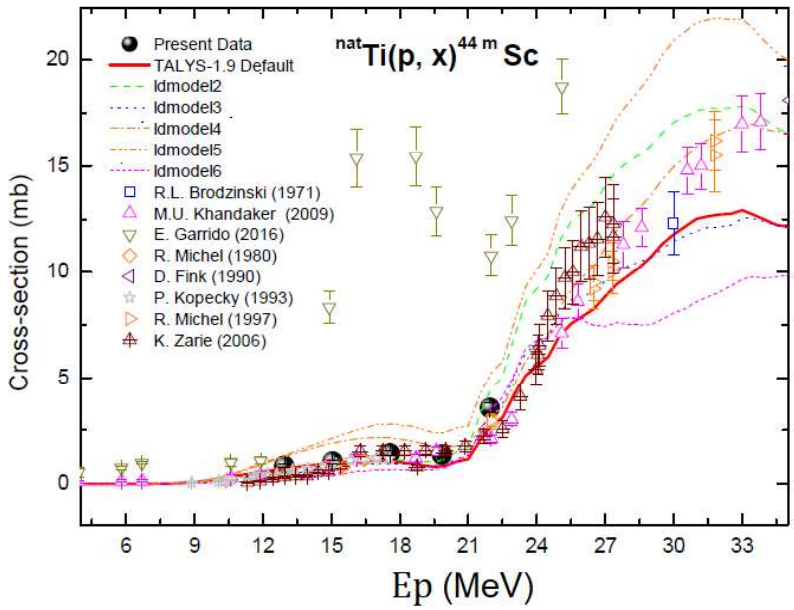

Figure 6.14: Excitation function of $^{nat}Ti(p,x)^{44m}Sc$ reaction. The comparison of the present and the literature data [61, 62, 64, 65, 67, 71, 72, 75] with different level density model parameters (ldmodel 1-6) [40–45] in TALYS-1.9 [37].

The excitation function of the $^{nat}Ti(p,x)^{47}Sc$ reaction is plotted in Fig. 6.10. It can be observed from the figure that the uncertainties have been minimized in present results as compared to literature data [61–64, 66, 71]. The present results were have also been found in agreement with the previous data. Fig. 6.10 also shows that the TALYS-1.9 level density model (ldmodel 1-5) [40–44] codes were able to reproduce the trend of the experimental results except the ldmodel 6, which was found to under-predict the data above 20 MeV energies. Fig. 6.11 present a comparison among the different level density models of ALICE-2014 (Fermi Gas, Obninsk and Kataria-Ramamurthy) with the default results of TALYS-1.9. A similar kind of trend can be observed for the Obninsk level density data values. The Fermi Gas and Obninsk models were found to reproduce the reaction cross-section data successfully, however, similar to the previous case, the Kataria-Ramamurthy level density under-predicted the data values above 18 MeV incident energies.

A comparison of the measured excitation function of the $^{nat}Ti(p,x)^{46}Sc$ reaction with the literature data, TALYS-1.9 and ALICE-2014 model codes are plotted in Figs. 6.12 and 6.13. The present results were found to follow the trend of the literature data [61, 63, 72, 74, 75]. It can be seen from the Fig. 6.12 that there are minor discrepancies among the data from Khandaker et al. [72] and Hermanne et al. [74], which may arise due to the choice of the flux monitor reactions. It can also be seen that the uncertainties in the present data have been optimized significantly compared to the literature data. Both TALYS-1.9 [37] and ALICE-2014 [38, 39] codes were found successful in order to reproduce the trend of the cross-section data for the considered energy range as shown in Fig. 6.13. However, a slight decrement is observed in ALICE-2014 values around 15 MeV as the $^{48}Ti(p,^{3}He)$ channel starts to contribute.

The excitation function of the $^{nat}Ti(p,x)^{44m}Sc$ reaction are shown in Figs. 6.14 and 6.15. The present data were compared with the literature data [61, 62, 64, 65, 67, 71, 72, 75], TALYS-1.9 [37] and the ALICE-2014 [38, 39] model codes. It can be seen from the figure 6.14 that the measured data are in fair agreement with the literature and theoretical data from TALYS-1.9. The data from Garrido et al. [75] do not follow the trend of the data reported by other authors as can be observed from figure 6.14. Fig. 6.15 shows a comparison of the present results with the theoretical data from ALICE-2014 code [38, 39]. It can be clearly stated that the model fails to reproduce the cross-section data. However, the predicted cross-sections were found to have an enhancement at two distinct places; one around 14 MeV and other above 22 MeV proton energies. These enhancements in the predicted data may be attributed to the contributions coming from the

$^{48}Ti(p, n\alpha)$ ($E_{th} = 14.17$ MeV) and $^{49}Ti(p, 2n\alpha)$ ($E_{th} = 22.47$ MeV) reaction channels, respectively. Further increasing trend of the cross-section may attribute to involvement of the $^{50}Ti(p, 3n\alpha)$ ($E_{th} = 33.63$ MeV) reaction.

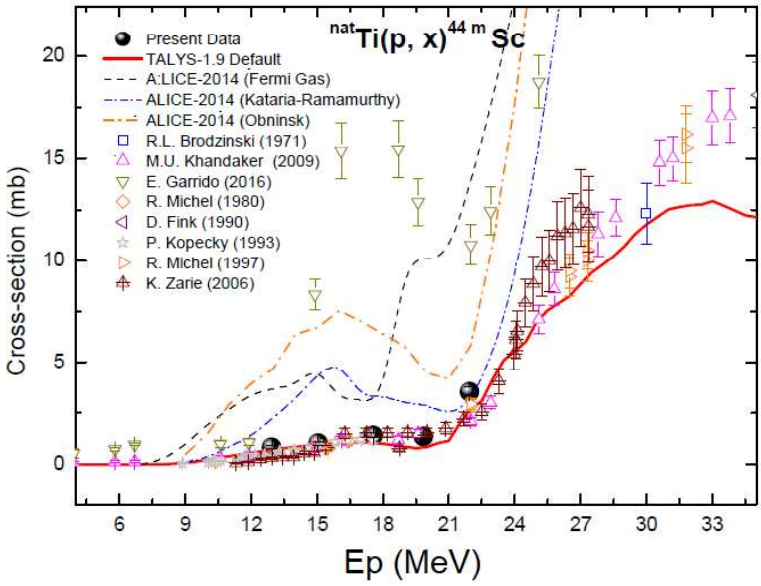

Figure 6.15: Excitation function of $^{nat}Ti(p, x)^{44m}Sc$ reaction. The comparison of the present and the literature data [61,62,64,65,67,71,72,75] with different level density model parameters (Fermi Gas and Kataria-Ramamurthy) in ALICE-2014 [38,39] and TALYS-1.9 [37] default values.

6.5 Pre-equilibrium Fraction Calculations

It is clear from the discussion provided in the previous section that the pre-equilibrium process plays an important role at the incident particle energies above $\approx$ 10 MeV for the reactions under consideration. Therefore, to investigate the contribution coming from the PE process into the formation of the reaction residues, we have calculated the PE fraction (%) presented by the equation 6.2. The PE calculations were performed in the framework of the nuclear model code TALYS-1.9 [37], by invoking suitable PE mode present within. The results of the model calculations for the $p +^{nat} Nb$ reactions are presented in Figures 6.16 and 6.17. It is observed from the figure that the results from the preeqmode 2 of the TALYS-1.9 [37] provide a better description of the measured data for the entire range under investigation for the ^{93m}Mo residue. Similarly, for the ^{92m}Nb radioisotope, the theoretical results were found to be in better agreement with the use of preeqmode 2.

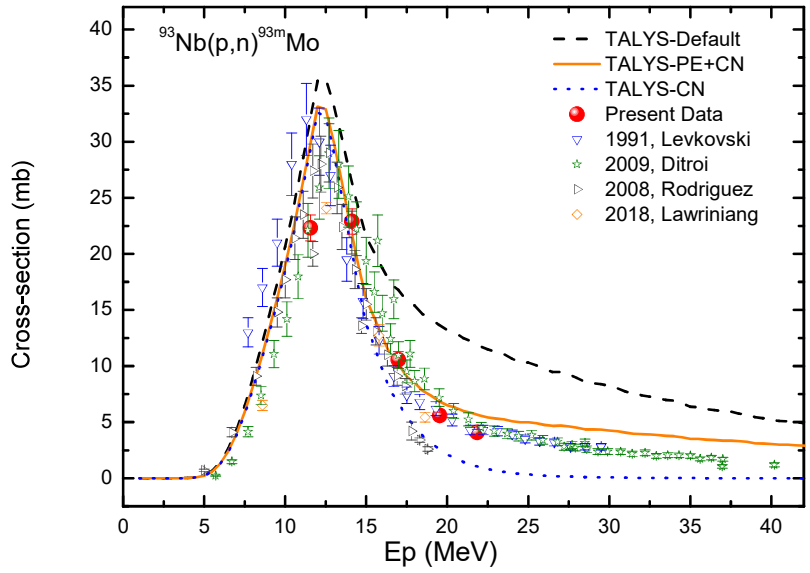

Figure 6.16: Excitation function of the $^{93}Nb(p,n)^{93m}Mo$ reaction. The comparison of the literature data [50–55] with pure CN and CN+PE reaction cross-sections from TALYS-1.9 [37]

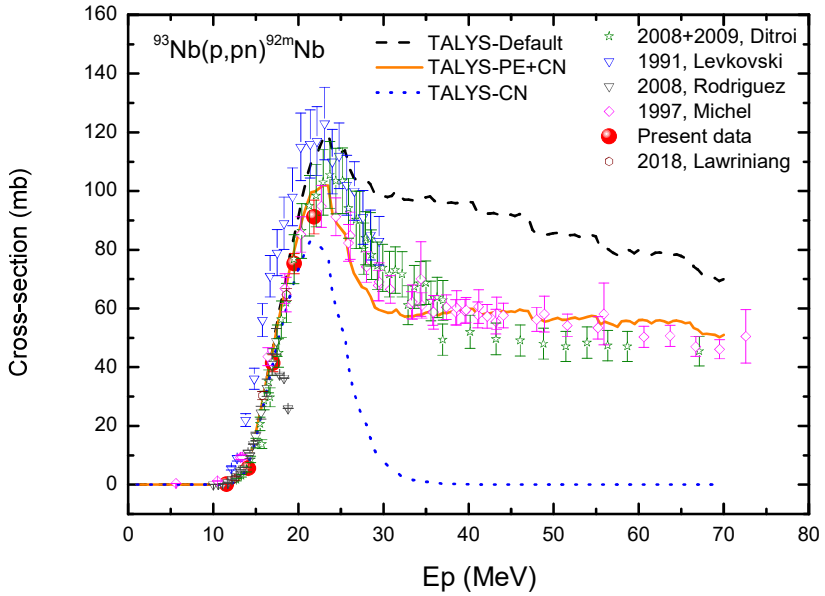

Figure 6.17: Excitation function of the $^{93}Nb(p,pn)^{92m}Nb$ reaction. The comparison of the literature data [50–55] with pure CN and CN+PE reaction cross-sections from TALYS-1.9 [37]

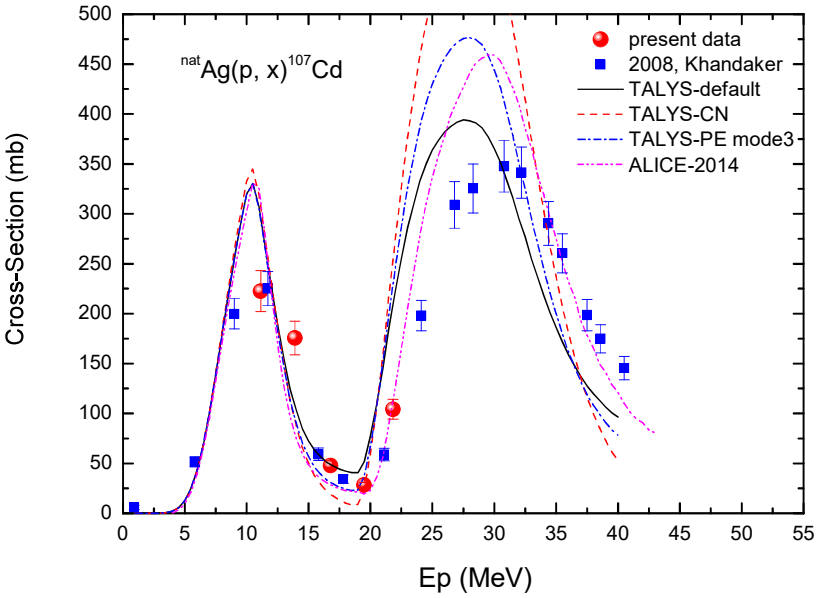

Figure 6.18: Excitation function of $^{nat}Ag(p,x)^{107}Cd$ reaction.. The comparison of the present and the literature data [60] with pure CN and CN+PE reaction cross-sections from TALYS-1.9 [37] and default values from ALICE-2014 [38,39].

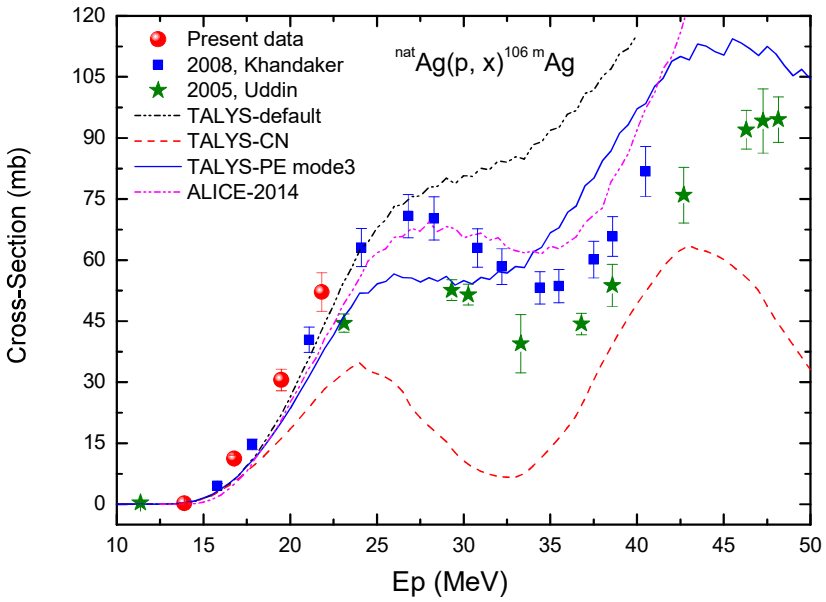

Figure 6.19: Excitation function of $^{nat}Ag(p,x)^{106m}Ag$ reaction. The comparison of the present and the literature data [56,60] with pure CN and CN+PE reaction cross-sections from TALYS-1.9 [37] and default values from ALICE-2014 [38,39].

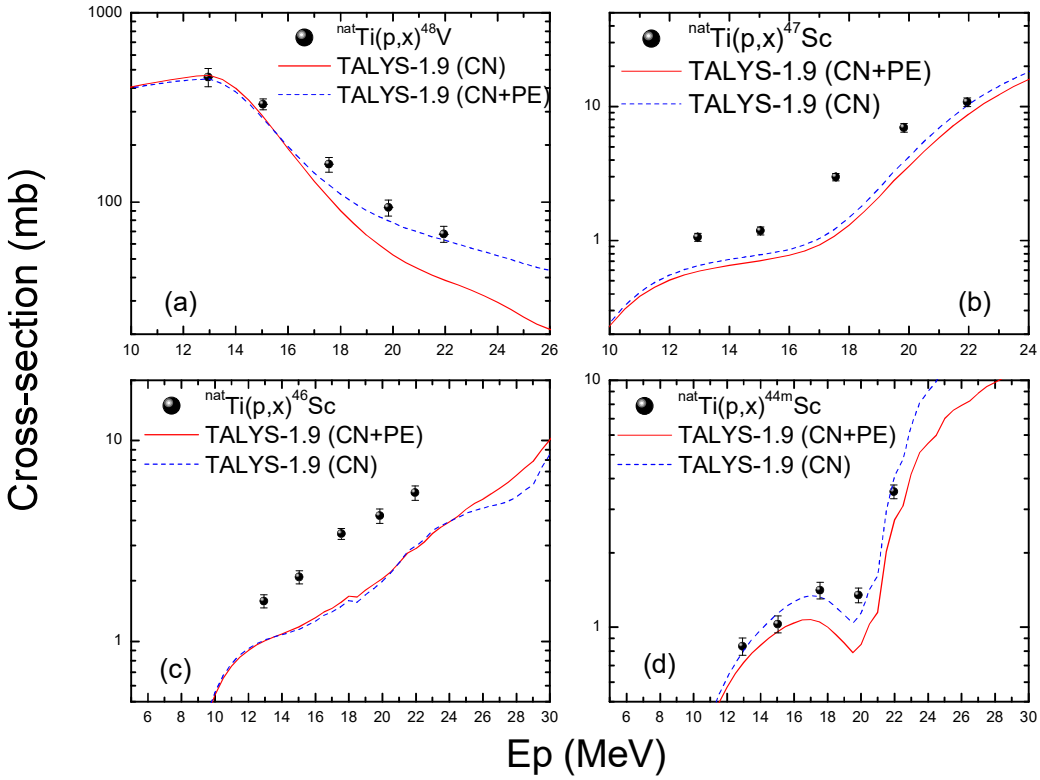

Figure 6.20: The comparison of the excitation function of the (a) $^{nat}Ti(p,x)^{48}V$, (b) $^{nat}Ti(p,x)^{47}Sc$, (c) $^{nat}Ti(p,x)^{46}Sc$, and (d) $^{nat}Ti(p,x)^{44m}Sc$ reactions in the present work with pure CN and CN+PE cross-sections from TALYS-1.9 [37].

The preeqmode 3 was used for find a better definition of the literature data for the ^{107}Cd and ^{106m}Ag radionuclide populated in the $p+^{nat}Ag$ reaction. A comparison of the results from TALYS-1.9 (with preeqmode 3) and ALICE-2014 (default) are shown in Figures 6.18 and 6.19, for the ^{107}Cd and ^{106m}Ag residues, respectively. It is obvious from the figures that the TALYS-1.9 is successful in order to find a better description for the literature data. A comparison between the present data and the PE results for the products formed in the $p+^{nat}Ti$ interaction are plotted in Figure 6.20. It can be observed from the figure that a significant PE contribution is present in the formation of the ^{48}V, ^{47}Sc, and ^{46}Sc radioisotopes. However, the CN description was found to be more satisfactory for the ^{44m}Sc isotope.

In view of the above discussion, PE fraction (PE %) has been calculated for each of the product nuclei produced in the proton induced reaction of ^{nat}Nb, Ag and Ti reactions. The results are presented in the Figure 6.21 for the respective cases. The percentage PE contribution was found to increase with the incident projectile energy for the ^{93m}Mo, ^{92m}Nb, and ^{106m}Ag radioisotopes. On the other hand,the PE contribution starts to increase at around 13 MeV and increases with the projectile energy and starts to die out

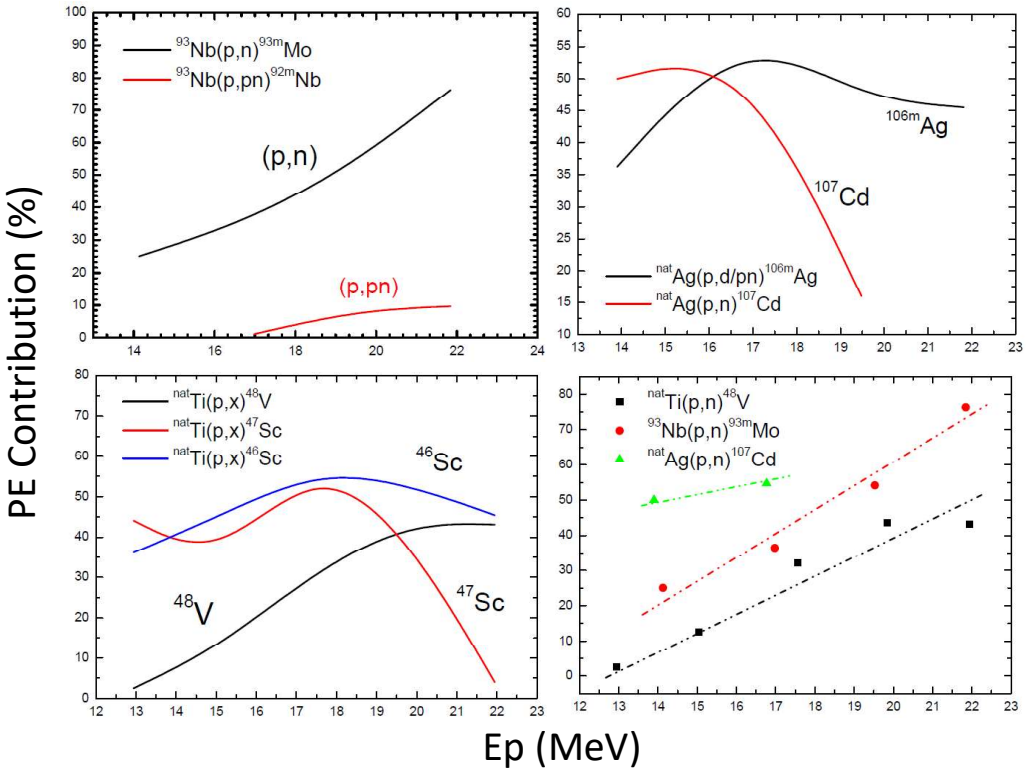

Figure 6.21: The estimated PE contribution (PE%) from the present data as a function of projectile energy.

for both the ^{107}Cd and ^{106m}Ag isotopes. The rapid decrease in PE% may be due to the opening up of $^{109}Ag(p,3n)^{107}Cd$ and $^{107}Ag(p,pn)^{106m}Ag$ channels. In case of the $p+^{nat}Ti$ reaction, the PE fraction starts to saturate/die out for ^{48}V and ^{46}Sc residues as the $^{50}Ti(p,3n)$ and $^{48}Ti(p,2pn)$ channels open up around 23 MeV proton energies. However, the PE fraction completely dies out for ^{46}Sc at the opening up of $^{49}Ti(p,2pn)$ channel around 20 MeV. Furthermore, the PE contribution was found to be greater in the reaction that consist a single neutron in the exit channel and has a small threshold value. This may be due to the probability of single particle emission in the PE mode is higher than the many-particle emission. It can also be stated that the PE emission inherently depends on the initial excitation energy or the Q-value of the reaction and dominate over the CN formation for higher excitation energies. Therefore, a comparison of the PE fractions among the (p, n) channels from all the three reactions [77,78] is also shown in figure 6.21. It is evident from the figure that the PE fraction depends on the associated Q-value of the reaction and decreases as with the increment in the $|Q|$-value.

✠ ✠ ✠ ✠

Bibliography

[1] D.R. Harries, Ferritic martensitic steels for use in near term and commercial fusion reactors, in: Proceedings of the Topical Conference on Ferritic Alloys for Use in Nuclear Energy Technologies, Snowbird, Utah, June 19-23, (1983).

[2] H. Padamsee, *RF Superconductivity for Accelerators*, John Wiley & Sons (1998).

[3] C. Rubbia, J. A. Rubio, S. Buono, F. Carminati, N. Fietier, J. Galvez, C. Geles, Y. Kadi, R. Klapisch, P. Mandrilion, J. P. Revol, and Ch. Roche, Conceptual design of a fast neutron operated high power energy amplifier, CERN Report No. CERN/AT/95-44 (ET), 1995, http://cds.cern.ch/record/289551/files/cern-0210391.pdf.

[4] C. D. Bowman et al.,Nuclear energy generation andwaste transmutation using and accelerator-driven intense thermal neutron source, International conference on emerging nuclear energy systems, Monterey, CA (United States), [Los Alamos National Laboratory Report No. LA-UR-91-2601] (1991).

[5] C. D. Bowman, Annu. Rev. Nucl. Part. Sci. **48**, 505 (1998).

[6] F. Carminati, R. Klapisch, J. P. Revol, Ch. Roche, J. A. Rubio, and C. Rubbia, An energy amplifier for cleaner and inexhaustible nuclear energy production driven by particle beam accelerator, CERN Report No. CERN/AT/93-47 (ET), 1993, http://cds.cern.ch/record/256520/files/at-93-047.

[7] The International Conference on Accelerator-Driven Transmutation Technologies and Applications, Las Vegas, 1994, edited by E. D. Arthur, S. A. Schriber, and A. Rodriguez, AIP Conf. Proc. No. 346 (AIP, New York, 1995).

[8] Accelerator driven systems: Energy generation and transmutation of nuclearwaste, status report, IAEA ReportNo. TECDOC- 985, 1997 (unpublished).

[9] S. Ganesan, Pramana J. Phys. **68**, (2007) 257.

[10] U. Fischer, P. Batistoni, E. Cheng, R. A. Forrest, T. Nishitani, *Proc. International conference on nuclear data for science and technology* vol **769** (AIP Conf.) (2005) 1478.

[11] V. Semkova, V. Avrigeanu, T. Glodariu, A.J. Koning, A.J.M. Plompen, D.L. Smith, S. Sudar, Nucl. Phys. A **730**, (2004) 255.

[12] C.L. Whitmarsh, Oak Ridge National Laboratory Report: ORNL-3281, UC-80-Reactor technology, TID-4500, 17th ed.

[13] J.W. Davis and D.L. Smith, J. Nucl. Mater. **85** & **86** (1979) 71.

[14] M. Fassbender, et al., Radiochim. Acta **87** (1999) 87.

[15] J.C. Blasko, P.D. Grimm, H. Ragde, Semin. Radiat. Oncol. 3(4) (October 1993) 240.

[16] C. Grignon et al., Nucl. Inst. Meth. Phys. Res. A **571**, (2007) 142.

[17] L. F. Masuner et al., App. Rad. Iso. **49** (4), (1998) 285.

[18] R. W. Baer et al.,American Journal of Physiology Heart and Circulatory Physiology **246** (3), (1984) H 418.

[19] A. P. Wehner et al., Lung clearance of neutron activated Mount St. Helens volcanic ash in the rat. Environmental Research **35** (1), (1984) 211.

[20] I. Mutsuo, K. Kazuhisa, Cosmogenic radionuclides in meteorites including recently fallen ones. Constraints on the exposure history of chondrites Chikyu Kagaku **35** (1), (inJapanese) (2001) 13.

[21] M.S. Uddin, M. Hagiwara, M. Baba, F. Tarkanyi, F. Ditroi, Appl. Radiat. Isot. **62** (2005) 533.

[22] M.S. Uddin, M. Hagiwara, F. Tarkanyi, F. Ditroi, M. Baba, Appl. Radiat. Isot. **60** (2004) 911.

[23] M.S. Uddin, M. Hagiwara, N. Kawata, T. Itoga, N. Hirabayashi, M. Baba, F. Tarkanyi, F. Ditroi, J. Csikai, J. Nucl. Sci. Tech. Suppl. 4 (2004) 160.

[24] F. Tarkanyi et al., IAEA-TECDOC-1211, Beam monitor reactions, charged particle cross-section database for medical radioisotope production, IAEA, Vienna. Austria (2001) http://www-nds.iaea.org/medical/S.

[25] B.P. Singh, M. K. Sharma, M. M. Musthafa, H. D. Bhardwaj, R. Prasad, *Nucl. Instrum. Methods A* **562** (2006) 717.

[26] A. Yadav, P. P. Sing, M. K. Sharma, D. P. Singh, Unnati, B. P. Singh, R. Prasad, M. M. Musthafa, Phys. Rev. C **78** (2008) 044606.

[27] I. A. Rizvi, K. Kumar, T. Ahmad, A. Agarwal, A. K. Chaubey, *Indian J Phys* **86** (10) (2012) 913.

[28] H. Kumar, S. A. Tali, M. A. Ansari, D. Singh, R. Ali, K. Kumar, N. P. M. Sathik, S. Parashari, A. Ali, R. Dubey, I. Bala, R. Kumar, R. P. Singh, S. Muralithar, *Nuclear Physics A* **960** (2017) 53.

[29] S. A. Tali, H. Kumar, M. A. Ansari, A. Ali, D. Singh, R. Ali, P. K. Giri, S. B. Linda, S. Parashari, R. Kumar, R. p. Singh, S. Muralithar, *Nuclear Physics A* **970** (2018) 208.

[30] J. F. Ziegler, *Nucl. Instrum. Methods B* **219** (2004) 1027, `http://www.srim.org/`.

[31] MAESTRO Multichannel Analyzer Emulation Software, ORTEC, **`https://www.ortec-online.com/products/application-software/maestro-mca`**

[32] Genie 2000 Gamma Analysis Software, MIRION Technologies, `https://www.mirion.com/products/genie-2000-gamma-analysis-software`.

[33] FitzPeaks Gamma Analysis and Calibration Software, Jim Fitzgerald, JF Computing Services, STANFORD IN THE VALE, Oxfordshire, SN78LE, `https://www.jimfitz.co.uk/fitzpeak.htm`.

[34] NuDat 2.7β 2011, *National Nuclear Data Center, Brookhaven National Laboratory*, `http://www.nndc.bnl.gov/`.

[35] Qtool: *calculation of reaction Q-values and threshold, Los Alamos National Library*, `http://cdfe.sinp.msu.ru/services/calc_thr/calc_thr.html`.

[36] G.F. Knoll, Radiation Detection and Measurement 3 rd edition (**Chapters 12 and 13**), John Wiley & Sons, (1999).

[37] A. J. Koning, S. Hilaire, S. Goriely, *TALYS user manual, A nuclear reaction program, NRG-1755 ZG PETTEN*, The Netherlands (2015).

[38] M. Blann, *Phys. Rev. Lett.* **28** (1972) 757.

[39] M. Blann, Code ALICE-91 PSR-146, *Statistical Model Code System with Fission Competition, Oak Ridge National Laboratory, Peripheral Shielding Routine Collection* (Livermore: Lawrence Livermore National Laboratory and IAEA) (1991).

[40] A. Gilbert, A. G. W. Cameron, *Can. J. Phys.* **43** (1965) 1446.

[41] W. Dilg, W. Schantl, H. Vonach, M. Uhl, *Nucl. Phys. A* **217** (1973) 269.

[42] A. V. Ignatyuk, K. K. Istekov, G. N. Smirenkin, *Sov. J. Nucl. Phys.* **29** 4 (1979) 450.

[43] A. V. Ignatyuk, J. L. Weil, S. Raman, S. Kahane, *Phys. Rev. C* **47** (1993) 1504.

[44] S. Goriely, S. Hilaire, A. J. Koning, *Improved microscopic nuclear level densities within the HFB plus combinatorial method, Phys. Rev. C* **78** (2008) 064307.

[45] S. Hilaire, M. Girod, S. Goriely, A. J. Koning, *Temperature dependent combinatorial level densities with the D1M Gogny force, to be published* (2013).

[46] A. J. Koning, M. C. Duijvestijn, *Nucl. Phys. A* **744** (2004) 15.

[47] H. Gruppelaar, P. Nagel, and P.E. Hodgson, Riv. Nuovo Cimento **9**, No. 7, (1986) 1.

[48] E. Gadioli and P.E. Hodgson, Pre-equilibrium nuclear reactions, Oxford Univ. Press (1992).

[49] M.K.Sharma et al., Phys. Rev. C **99**, (2019) 014608.

[50] F. Ditrói, S. Takács, F. Tárkányi, M. Baba, E. Corniani, Y. N. Shubin, *Nucl. Instrum. Methods B* **266** (2008) 5087.

[51] M. A. Avila-Rodriguez, J. S. Wilson, M. J. Schueller, S. A. McQuarrie, *Nucl. Instrum. Methods B* **266** (2008) 3353.

[52] F. Ditró, A. Hermanne, E. Corniani, S. Takács, F. Tárkányi, J. Csikai, Y. N. Shubin, *Nucl. Instrum. Methods B* **267** (2009) 3364.

[53] V. N. Levkovski, *Activation Cross Sections by Protons and Alphas*, Inter-Vesi, Moscow (1991).

[54] R. Michel, R. Bodemann, H. Busemann, Ret al., *Nucl. Instrum. Methods B* **129** (1997) 153.

[55] B. Lawriniang, R. Ghosh, S. Badwar, V. Vansola, Y. S. Sheela, S. V. Suryanarayana, H. Naik, Y. P. Naik, B. Jyrwa, *Nucl. Phys. A* **973** (2018) 79.

[56] M. U. Khandaker, K. Kim, K.-S. Kim, M. Lee, G. Kim, Y. S. Cho, Y. O. Lee, *Nucl. Instrum. Methods in Physics Res.*, Sect. B, **266** (2008) 5101.

[57] IAEA-EXFOR Experimental nuclear reaction data base, http://www.nds.iaea.org/exfor.

[58] M. S. Uddin, M, Hagiwara, F. Tarkanyi, F. Ditroi, M. Baba, *Appl. Radiat. Isot.* **60**, (2004) 911.

[59] M. S. Uddin, M, Hagiwara, N. Kawata, T. Itoga, N. Hirabayashi, M. Baba, F. Tarkanyi, F. Ditroi, J. Csikai, *J. Nucl. Sci. Tech. Supplement* **4**, (2004) 160.

[60] M. S. Uddin, M. Hagiwara, M. Baba, F. Tarkanyi, F. Ditroi, *Applied Radiation and Isotopes* **62** (2005) 533.

[61] R.L. Brodzinski et al., Phys. Rev. C **4**, (1971) 1250.

[62] D. Fink et al.,Nucl. Inst. Meth. B **52**, (1990) 601.

[63] P. Jung, Conference on Nuclea Data for Science and Technology, Juelich, Exfor D4058028 (1991) 352.

[64] P. Kopecky et al., App. Rad. Isot. **44** (4), (1993) 687.

[65] R. Michel et al., Nucl. Inst. Meth. B **129**, (1997) 153.

[66] R. Michel et al.,Journal of Inorganic & Nuclear Chemistry **40** (11), (1978) 1845.

[67] R. Michel, G. Brinkmann, Journal of Radioanalytical and Nuclear Chemistry **59** (2), (1980) 467.

[68] F. Szelecsenyi et al., Nucl. Inst.Meth. Phys. Res. B **174**, (2001) 47.

[69] F. Tarkanyi et la., Conference on Nuclear Data for Science and Technology, Juelich, Exfor D4080003 (1991) 529.

[70] S. Takacs et al., Nucl. Inst.Meth. Phys. Res. B **188**, (2002) 106.

[71] K. Zarie et al., Radiochim. Acta. **94** (12) (2006) 795.

[72] M.U. Khandaker et al., Applied Radiation and Isotopes **67** (2009) 1348.

[73] M.E. Bennett et al., Nucl. Instrum. Methods Phys. Res., Sect. B **276** (2012) 62.

[74] A. Hermanne et al., Nuclear Instruments and Methods in Physics Research B **338** (2014) 31.

[75] E. Garrido et al., Nuclear Instruments and Methods in Physics Research B **383** (2016) 191.

[76] J.R. Huizenga, L.G. Moretto, Annu. Rev. Nucl. Sci. 22 (1972) 427.

[77] S. Parashari et al., Nucl. Phys. A **978** (2018) 160.

[78] S. Parashari et al., Nucl. Phys. A **979** (2018) 102.